Accelerated and Stabilized Meshfree Method for Impact-Blast Modeling

J. S. Chen, Ph.D., M.ASCE[1]; Jonghyuk Baek[2]; Tsung-Hui Huang[3]; and Michael C. Hillman, Ph.D.[4]

[1]Dept. of Structural Engineering, UC San Diego, La Jolla, CA. E-mail: js-chen@ucsd.edu
[2]Dept. of Structural Engineering, UC San Diego, La Jolla, CA. E-mail: job011@ucsd.edu
[3]Dept. of Structural Engineering, UC San Diego, La Jolla, CA. E-mail: tsh011@ucsd.edu
[4]Dept. of Civil and Environmental Engineering, Pennsylvania State Univ., PA. E-mail: mhillman@psu.edu

ABSTRACT

Meshfree methods such as the reproducing kernel particle method (RKPM) are well suited for modeling materials and solids undergoing fracture and damage processes, and nodal integration is a natural choice for modeling this class of problems. However, nodal integration suffers from spatial instability, and the excessive material deformation and damage process could also lead to kernel instability in RKPM. This paper reviews the recent advances in nodal integration for meshfree methods that are stable, accurate, and with optimal convergence. A variationally consistent integration (VCI) is introduced to allow correction of low order quadrature rules to achieve optimal convergence, and several stabilization techniques for nodal integration are employed. The application of the stabilized RKPM with nodal integration for shock modeling, fracture to damage multiscale mechanics, and materials modeling in extreme events, are demonstrated. These include the modeling of man-made disasters such as fragment-impact processes, penetration, shock, and blast events will be presented to demonstrate the effectiveness of the new developments.

1. INTRODUCTION

Reproducing Kernel Particle Method (RKPM) has shown to be effective for large deformation problems (Chen et al. 1996) owing to its node-based discretization and Reproducing Kernel (RK) approximation with flexibility in controlling locality, continuity, and completeness. The recent advances in nodal integration with proper enforcement of variational consistency and stabilization makes RKPM a truly meshfree method applicable to a wide range of continuum to discrete-particle like mechanics problems. The early work of the Stabilized Conforming Nodal Integration (SCNI) (Chen et al. 2001) introduced the concept of integration constraint in a form of numerical divergence condition to ensure the first order Galerkin exactness, consistent with the first order of completeness with linear basis in the trial functions, for passing linear patch test and achieving optimal convergence. The strain smoothing introduced in SCNI employed a contour integral on a conforming cell for evaluation of nodal gradient while meeting the numerical divergence condition. Several variants of SCNI with strain smoothing have been proposed since then, including the smoothed finite element method (Liu et al. 2007), the 2nd order accurate smoothed strain type quadrature rule (Duan et al. 2012), the variationally consistent integration (VCI) for arbitrary order of Galerkin exactness (Chen et al. 2013), among others. The VCI approach has also been used as a correction of any quadrature rules such as direct nodal integration (DNI) or stabilized non-confirming nodal integration (SNNI) to achieve optimal rates of convergence. Additionally, several stabilization methods for meshfree methods with nodal integrations have been proposed. These include the gradient SCNI (G-SCNI) (Chen et

al. 2007b) with employment of implicit gradients embedded in the RK approximation as a stabilization of SCNI, and the naturally stabilized nodal integration (NSNI) (Hillman and Chen 2016) by introducing Taylor expansion of nodal strain calculated with implicit gradient. These stabilized nodal integration techniques with node-based approximation and discretization form an effective computational paradigm for modeling problems involving severe material deformation, damage, and fragmentation in the extreme events. This paper summarizes the semi-Lagrangian RK approximation, the SCNI and Variational Consistency (VC) corrected SNNI, called VC-SNNI, as well as NSNI stabilization, and demonstrates their effectiveness in modeling contact-impact, bullet penetration, blast, and explosive welding processes.

2. SEMI-LAGRANGIAN RK APPROXIMATION

Let a domain $\Omega \in \mathbb{R}^d$ be discretized by a set of NP nodes, $\{\mathbf{x}_I \,|\, \mathbf{x}_I \in \Omega\}_{I=1}^{NP}$, where $\mathbf{x}_I$ is the material coordinate of node I. In a discrete reproducing kernel (RK) approximation, an RK shape function, $\Psi_I(\mathbf{x})$, is defined on a compact support of node I, as shown in Figure 1.

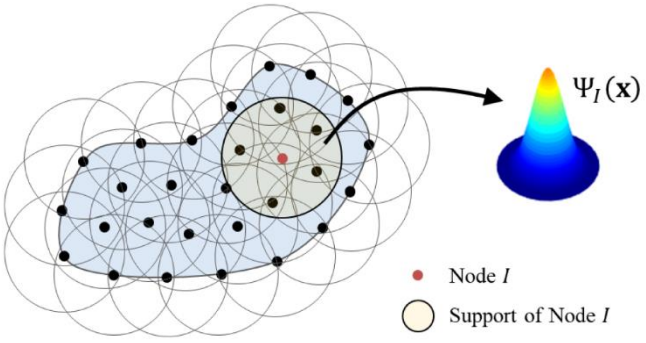

Figure 1. 2D illustration of meshfree nodal discretization, kernel support, and RK shape function – courtesy of UC San Diego.

The discrete RK approximation, $\mathbf{u}^h(\mathbf{x})$, of a function $\mathbf{u}(\mathbf{x})$ is defined as (Liu et al. 1995; Chen et al. 1996; Huang et al. 2019b)

$$\mathbf{u}^h(\mathbf{x}) = \sum_{I=1}^{NP} \Psi_I(\mathbf{x})\mathbf{u}_I, \tag{1}$$

where $\mathbf{u}_I$ is the nodal coefficient of node I. The shape function, $\Psi_I(\mathbf{x})$, is obtained by considering a set of reproducing conditions up to an order n as follows:

$$\sum_{\mathrm{I}=1}^{NP} \Psi_I(\mathbf{x})\mathbf{x}_I^{\boldsymbol{\alpha}} = \mathbf{x}^{\boldsymbol{\alpha}}, \;\; |\boldsymbol{\alpha}| \le n, \tag{2}$$

where $\boldsymbol{\alpha} = (\alpha_1, \alpha_2, ..., \alpha_d)$, is a multi-index with dimension d, $\mathbf{x}^{\boldsymbol{\alpha}} = x_1^{\alpha_1} \cdot x_2^{\alpha_2} \cdot \cdots \cdot x_d^{\alpha_d}$, and $|\alpha| = \sum_{i=1}^{d} \alpha_i$. The resulting RK shape function reads

$$\Psi_I(\mathbf{x}) = \mathbf{H}(\mathbf{0})\mathbf{M}^{-1}(\mathbf{x})\mathbf{H}(\mathbf{x}-\mathbf{x}_I)\Phi_a(\mathbf{x}-\mathbf{x}_I), \tag{3}$$

where the basis vector $\mathbf{H}(\mathbf{x})$ is

$$\mathbf{H}(\mathbf{x}) = \begin{bmatrix} 1 & x_1 & x_2 & \cdots & x_d^n \end{bmatrix}^T, \tag{4}$$

the moment matrix $\mathbf{M}(\mathbf{x})$ is

$$\mathbf{M}(\mathbf{x}) = \sum_{I=1}^{NP} \mathbf{H}(\mathbf{x}-\mathbf{x}_I)\mathbf{H}^{\mathrm{T}}(\mathbf{x}-\mathbf{x}_I)\Phi_a(\mathbf{x}-\mathbf{x}_I), \tag{5}$$

and $\Phi_a(\mathbf{x}-\mathbf{x}_I)$ is the kernel function with support size a, where $a = ch$ with the normalized support size c and nodal spacing h. Kernel functions with different order of continuities, such as B-spline functions, can be employed for desired smoothness in the RK approximation (Liu et al. 1995; Chen et al. 2017). The order of RK approximation is determined by the polynomial completeness adopted in the basis vector $\mathbf{H}$ whereas the smoothness of the approximation is controlled by the employed kernel function. The completeness and the smoothness of the solution space can be chosen and combined in a flexible manner (Chen et al. 2017). In the semi-Lagrangian RK approximation (Chen and Wu 2007a), the reproducing conditions are constructed in the current configuration, where the nodal neighbor list is updated by redefining the kernel support coverage. In this way, the nodal points follow the motion of material points under a Lagrangian description, while the mesh distortion issues associated with conventional mesh-based methods are effectively avoided (Guan et al. 2009; Chi et al. 2015; Sherburn et al. 2015; Wei et al. 2019)

3. STABILIZED NODAL INTEGRATION

In meshfree methods, Gaussian integration using background cells is prohibitively expensive (Chen et al. 2001; Babuška et al. 2008; Dolbow and Belytschko 1999; Chen et al. 2013), and detracts from the meshfree nature of the formulation. Therefore, node-based quadrature is preferred, particularly for large-deformation formulations such as the semi-Lagrangian framework presented in Section 2, so that state and field variables live and are updated at the nodal locations. However, direct nodal integration yields low accuracy, as well as unstable solutions (Chen et al. 2001; Chen et al. 2013; Beissel and Belytschko 1996).

3.1 Variationally Consistent Nodal Integration

To remedy this situation, the so-called integration constraint has been introduced, which is the requirement to obtain first-order Galerkin exactness, or in other words, to pass the linear patch test (Chen et al. 2001):

$$\hat{\int_{\Omega}} \nabla \hat{\Psi}_I \mathrm{d}\Omega = \hat{\int_{\partial\Omega}} \hat{\Psi}_I \mathbf{n}\mathrm{d}\Gamma, \tag{6}$$

where "^" over the integral symbol denotes numerical integration. To achieve the above, a stabilized conforming nodal integration has been proposed (Chen et al. 2001). In this approach, shape function gradients are smoothed over conforming representative nodal domains which partition the domain Ω, as shown in Figure 2(a-b).

This stabilizes the solution by avoiding direct derivatives at nodal locations, and also satisfies (6) by converting the smoothing operation to boundary integration using the divergence theorem:

$$\tilde{\nabla}\Psi_I(\mathbf{x}_L) = \frac{1}{V_L}\int_{\Omega_L} \nabla \Psi_I \mathrm{d}\Omega = \frac{1}{V_L}\int_{\partial\Omega_L} \Psi_I \mathbf{n}\mathrm{d}\Gamma, \tag{7}$$

where $\tilde{\nabla}$ denotes the smoothed gradient operation, Ω_L is the representative domain of node $\mathbf{x}_L$, $V_L = |\Omega_L|$ is the volume of the domain, and $\mathbf{n}$ is the normal of the surface $\partial\Omega_L$. It is easy to show that the conforming property of the nodal domains ensures (6) is satisfied.

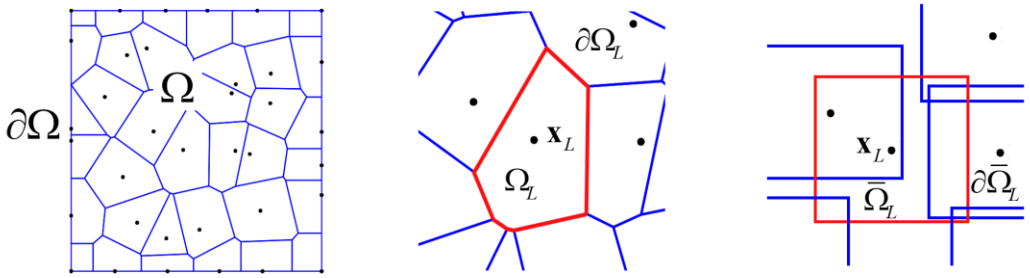

Figure 2. (a) Partition of domain Ω into conforming nodal domains, (b) conforming nodal domain, (c) non-conforming nodal domain – courtesy of the Pennsylvania State University.

However, in extreme deformation simulations, it would be necessary to reconstruct conforming nodal domains, which is cumbersome and CPU intensive. Thus, a non-conforming smoothing approach in the stabilized non-forming nodal integration (SNNI) has been introduced to avoid this difficulty (Guan et al. 2011), and this approach is depicted in Figure 2 (c). However, relaxing the conformity of cells in SNNI results in the violation of the constraint (6), and inaccurate, non-convergent solutions are obtained (Chen et al. 2013).

To rectify this situation, an arbitrary-order variationally consistent integration has been introduced (Chen et al. 2013), which allows gradients be constructed by non-conforming nodal domains to pass the patch test. This is achieved by recognizing that the requirement in (6) strictly pertains to the test functions. Therefore, a Petrov-Galerkin approach is introduced, where trial function gradients are constructed via straight-forward smoothing over non-conforming domains

$$\tilde{\nabla}\Psi_I(\mathbf{x}_L)=\frac{1}{\bar{V}_L}\int_{\bar{\Omega}_L}\nabla\Psi_I\,\mathrm{d}\bar{\Omega}=\frac{1}{\bar{V}_L}\int_{\partial\bar{\Omega}_L}\Psi_I\mathbf{n}\,\mathrm{d}\bar{\Gamma}, \tag{8}$$

where $\bar{\Omega}_L$ is the non-conforming representative domain of node $\mathbf{x}_L$, $\bar{V}_L=|\bar{\Omega}_L|$ is the volume of that domain, and $\partial\bar{\Omega}_L$ is the surface of that domain.

The test functions are also first constructed as (8), with a correction introduced as follows:

$$\hat{\nabla}\Psi_I(\mathbf{x}_L)=\tilde{\nabla}\Psi_I(\mathbf{x}_L)+\xi_I\Theta_I(\mathbf{x}_L), \tag{9}$$

where $\hat{\nabla}$ denotes the corrected gradient, ξ_I is a vector of coefficients to be determined, and Θ_I is a correction function defined as

$$\Theta_I(\mathbf{x})=\begin{cases}1 & \text{if } \mathbf{x}\in\mathrm{supp}(\Psi_I(\mathbf{x}))\\ 0 & \text{else}\end{cases}, \tag{10}$$

where $\mathrm{supp}(\Psi_I(\mathbf{x}))$ denotes the support of the shape function $\Psi_I(\mathbf{x})$. The coefficients ξ_I are solved for by substitution of (9) into (6) yielding:

$$\xi_{Ii}=\left(\int_{\Omega}\Theta_I\,\mathrm{d}\Omega\right)^{-1}\left(\int_{\partial\Omega}\Psi_I\mathbf{n}\,\mathrm{d}\Gamma-\int_{\Omega}\tilde{\nabla}\Psi_I\,\mathrm{d}\Omega\right)_i, \tag{11}$$

The variational consistent (VC) correction described above has been applied to the correction of SNNI, called the VC-SNNI (Chen et al. 2013).

3.2. Naturally Stabilized Nodal Integration

The gradient-smoothing technique (8) precludes the instability associated with zero-energy modes. However, small-wavelength modes with very low energy can still exist in the solution

(Chen et al. 2007b; Puso et al. 2008). An implicit gradient stabilization called naturally stabilized nodal integration (NSNI) has been proposed (Hillman and Chen 2016) based on Taylor series expansion of the strains, which employs implicit gradients (Chen et al. 2004; Chi et al. 2013) to avoid computationally intensive explicit computation of higher order derivatives.

In this approach, the strain $\boldsymbol{\varepsilon}$ around a node $\mathbf{x}_L$ is expanded as:

$$\boldsymbol{\varepsilon}(\mathbf{x}) \approx \boldsymbol{\varepsilon}(\mathbf{x}_L) + \sum_{i=1}^{3} (x_i - x_{Li}) \boldsymbol{\varepsilon}_{,i}(\mathbf{x}_L), \tag{12}$$

Under the gradient-smoothing framework introduced in Section 3.1, the smoothed strain $\tilde{\boldsymbol{\varepsilon}}$ evaluated at a node is computed as:

$$\tilde{\boldsymbol{\varepsilon}}(\mathbf{x}_L) = \frac{1}{2\bar{V}_L} \int_{\partial\bar{\Omega}_L} \mathbf{u}^h \otimes \mathbf{n} + \mathbf{n} \otimes \mathbf{u}^h \mathrm{d}\bar{\Gamma}, \tag{13}$$

In order to avoid direct differentiation of the strains, implicit gradients (Chen et al. 2004) are introduced, which have the same computational cost as computing the shape function itself. In conjunction with strain-smoothing, the differentiation in (13) is approximated as:

$$\boldsymbol{\varepsilon}_{,i}(\mathbf{x}_L) \approx \frac{1}{2\bar{V}_L} \int_{\partial\bar{\Omega}_L} \hat{\mathbf{u}}_i^h \otimes \mathbf{n} + \mathbf{n} \otimes \hat{\mathbf{u}}_i^h \mathrm{d}\bar{\Gamma}, \tag{14}$$

where

$$\hat{\mathbf{u}}_i^h(\mathbf{x}_L) = \sum_I \Psi_{Ii}^{\nabla}(\mathbf{x}_L) \mathbf{u}_I, \tag{15}$$

and Ψ_{Ii}^{∇} is the implicit gradient shape function (Chen et al. 2004; Chi et al. 2013):

$$\Psi_{Ii}^{\nabla}(\mathbf{x}) = \mathbf{D}_i \mathbf{M}^{-1}(\mathbf{x}) \mathbf{H}(\mathbf{x} - \mathbf{x}_I) \Phi_a(\mathbf{x} - \mathbf{x}_I), \tag{16}$$

where $\mathbf{D}_i = -\begin{bmatrix} 0 & \delta_{i1} & \delta_{i2} & \delta_{i3} & 0 & \cdots & 0 \end{bmatrix}^T$.

Substituting (12) for the virtual strains near each node, and performing the same expansion procedures for the Cauchy stress following (Hillman and Chen 2016), one obtains the stabilized internal force at each node $\mathbf{f}_I^{\text{int}}$ for the updated Lagrangian formulation:

$$\mathbf{f}_I^{\text{int}} = \mathbf{f}_I^{ss} + \mathbf{f}_I^{ns}. \tag{17}$$

Here, $\mathbf{f}_I^{ss}$ is the internal force performed using standard strain smoothing:

$$\mathbf{f}_I^{ss} = \sum_{L=1}^{NP} \tilde{\mathbf{B}}_I^{\mathrm{T}}(\mathbf{x}_L) \boldsymbol{\tau}(\mathbf{x}_L) V_L, \tag{18}$$

where $\tilde{\mathbf{B}}_I$ is the strain-gradient matrix in Voigt notation associated with (13), $\boldsymbol{\tau}$ is the Cauchy stress in Voigt notation. $\mathbf{f}_I^{\text{ns}}$ is the naturally stabilized portion of the internal force:

$$\mathbf{f}_I^{\text{ns}} = \sum_{i=1}^{d} \sum_{L=1}^{NP} \hat{\mathbf{B}}_{Ii}^{\mathrm{T}}(\mathbf{x}_L) \hat{\boldsymbol{\tau}}_i(\mathbf{x}_L) M_{Li}, \tag{19}$$

where $\hat{\mathbf{B}}_{Ii}$ is the approximation to the derivative of $\tilde{\mathbf{B}}_I$ with respect to x_i, in Voigt notation, M_{Li} is the second moment of inertia with respect to the nodal domain of $\mathbf{x}_L$ and direction x_i, and $\hat{\boldsymbol{\tau}}_i$ is the approximation to the derivative of the Cauchy stress with respect to x_i. The calculation of the "pseudo-stress" $\hat{\boldsymbol{\tau}}_i$ is performed following (Hillman and Chen 2016).

With (17) in hand, the calculation proceeds following the standard predictor-corrector

algorithm of the explicit Newmark-β method, with lumped mass. The implicit gradient stabilization (NSNI) is applied to the VC-SNNI, referred as the VC-NSNI (Hillman and Chen 2016).

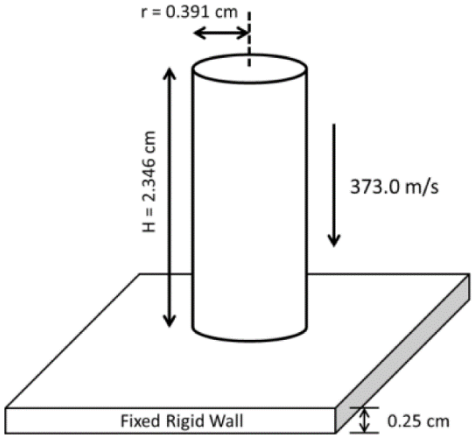

Figure 3. Problem set-up for the Taylor bar impact problem – courtesy of UC San Diego.

4. NUMERICAL EXAMPLES

Several numerical examples are analyzed to examine the performance of the RKPM approach shown in Section 2 to 3 for impact-blast Modeling.

Table 1. Model constants for Taylor bar impact problem

Parameters	Value
Young's modulus	78.20 GPa
Possion's ratio	0.30
Density	2700 kg/m^3
Yield strength	270 MPa

4.1. Taylor Bar Impact

The Taylor bar impact problem (Taylor 1948) is first employed as the demonstration problem. An aluminum bar with an initial height and radius of 2.346 cm and 0.391 cm, respectively, impacts a rigid wall with an initial velocity of 373.0 m/s, as shown in Figure 3. For the aluminum material, J2 plasticity with isotropic hardening is considered, and material properties are listed in Table 1. A quartic B-Spline rectangular kernel with a normalized support size of 2.0 is employed for the RK approximation

The yield stress of the rod is taken as $K\left(\bar{e}_p\right)=\sigma_Y\left(1+125\bar{e}_p\right)^{0.1}$, where σ_Y is initial yield strength and $\bar{e}_p$ is the equivalent plastic strain. The kernel contact algorithm (Chi et al. 2015) is adopted to capture the interaction between the bar and the fixed frictionless wall. For comparison purpose, RKPM with three nodal integration schemes (SNNI, NSNI, and VC-NSNI) are employed here.

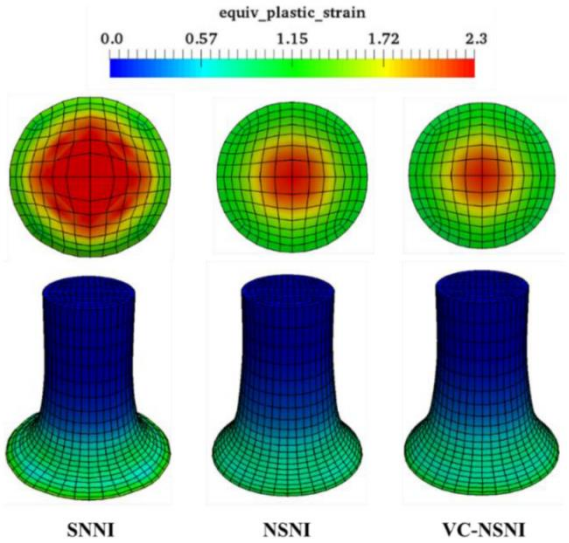

Figure 4. Equivalent plastic strain field of the Taylor bar at 40 microseconds obtained by RKPM with different quadrature schemes – courtesy of UC San Diego.

Table 2. Height and radius of the deformed Taylor bar

	Height (cm)	Radius (cm)
RKPM (SNNI)	1.653	0.792
RKPM (NSNI)	1.650	0.723
RKPM (VC-NSNI)	1.651	0.745
FEM (Wilkins et al, 1973)	1.652	0.742
Experiment (Wilkins et al, 1973)	1.651	-

From Figure 4, spurious oscillatory modes appear in the equivalent plastic strain distribution on the bar bottom face in the SNNI solution, while NSNI and VC-NSNI demonstrate stable solutions. The height and radius of the deformed bar for the three quadrature schemes are given in Table 2, along with reference FEM solutions and experimental data. It can be seen that, while all formulations provide reasonable prediction of the deformed heights, the results of VC-NSNI is the most accurate compared to the reference solutions.

4.2. Bullet Penetration

A CorTuf ultra high-strength concrete panel is subject to an impact of a spherical ASTM A681 steel bullet. The target panel is 304.8 mm × 304.8 mm with a thickness of 14.3 mm. The radius of the bullet is 12.7 mm. The initial velocity of the bullet is approximately 462.1 m/s. The material behavior of steel is modeled by J2 plasticity with isotropic hardening with density ρ =7,806 kg/m^3, Young's modulus E =200 GPa, Poisson's ratio ν =0.26, yield stress σ_Y =2,400 MPa, and hardening modulus H =2,500 MPa. The material behavior of concrete is modeled by MIDM (microcrack informed damage model)-enhanced AFC model (Ren et al. 2011), and the model parameters follow (Chen et al. 2011). The concrete panel and the steel bullet are discretized by 107,811 and 1,516 RK nodes, respectively. The semi-Lagrangian RKPM is employed with normalized support sizes of 1.4 and 2.8 for the concrete panel and the steel pullet, respectively. Also, the linear basis with a quartic spline is used. For the numerical integration, VC-NSNI is used.

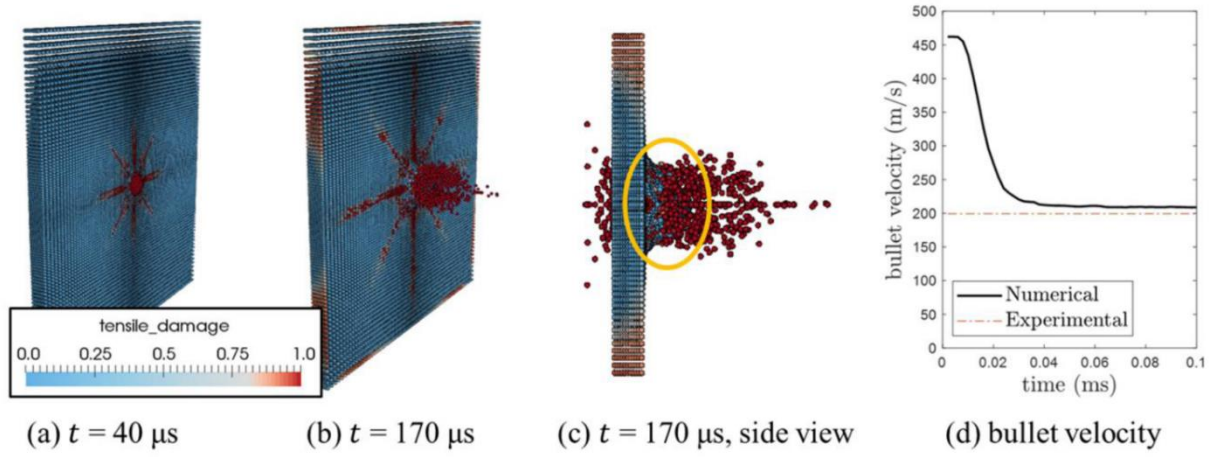

Figure 5. RKPM results of bullet penetration: (a)-(b) progressive deformation with tensile damage field, exit-face view; (c) side view; (d) bullet velocity profile – courtesy of UC San Diego.

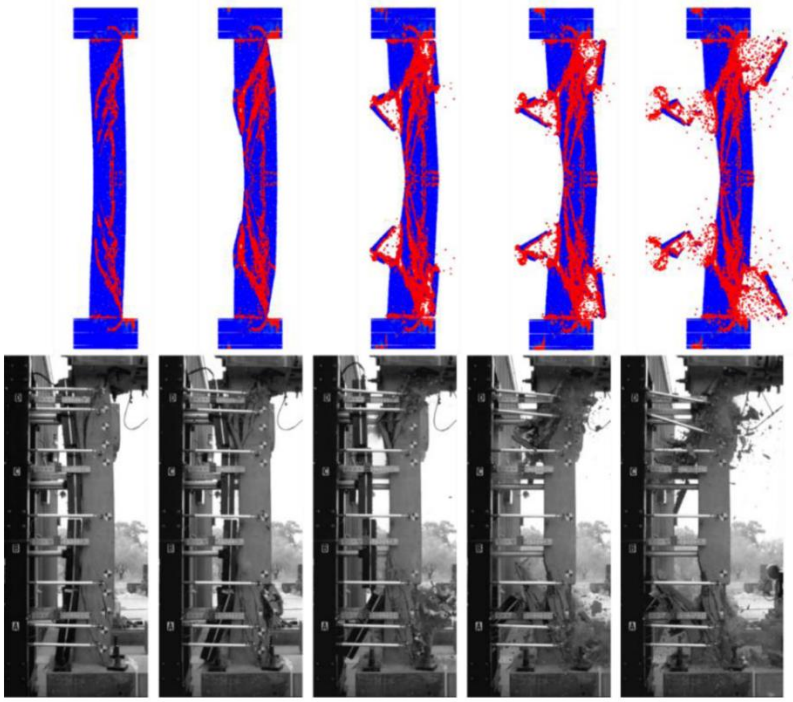

Figure 6. Progressive failure process: Top, numerical result obtained by RKPM simulation (courtesy of UC San Diego); Bottom, high-speed video frames of the reinforced concrete column subject to blast loading (Hegemier et al. 2006).

Figure 5 (a) and (b) show progressive deformation of the concrete panel with the tensile damage field. The radial propagation of damage and the cloud of spalling particles are well-captured. As shown in Figure 5 (c), the RKPM formulation with VC-NSNI also well captures the generation of larger concrete debris, which is important in the evaluation of spall-induced secondary damages on people and assets behind the panel. Additionally, as shown in Figure 5 (d), the numerically predicted exit velocity of the bullet has a reduction of approximately 55 %, which agrees well with the experimentally measured velocity reduction of approximately 57 %.

4.3. Blast Impact on Concrete Column

A reinforced concrete (RC) column subject to blast loading is modeled. The blast loading profile is obtained from the hydraulic/high pressure nitrogen-based UCSD blast simulator which can simulate full-scale explosive loads (Hegemier et al. 2006). The RC column is model by MIDM-enhanced AFC concrete model (Ren et al. 2011) with embedded rebars with J2 plasticity. The semi-Lagrangian RKPM is employed with normalized support sizes of 2.0. Also, the linear basis with a cubic B-spline is used. For the numerical integration, VC-NSNI is used. As shown in Figure 6, the column fractures under the blast loading, accompanied by post-blast spalling and debris near the top and bottom supports. RKPM demonstrates satisfactory capability in capturing the progressive structural failure process when compared with the frame sequence from a high-speed video record (Hegemier et al. 2006).

4.4. Explosive Welding

An explosive welding experiment (Bahrani and Crossland 1964) of a 0.8-mm-thick stainless-steel flyer plate and a 1.2-mm-thick mild steel base plate with an initial angle of 6 ° is modeled as shown in Figure 7 (Baek et al. 2019). The flyer plate is driven by a 3.2-mm-thick PETN-based sheet explosive. The length of plates and explosive is 12 mm. For numerical modeling, the plane strain condition is assumed. The explosive is modeled by the Jones-Wilkins-Lee equation of state, and the Johnson-Cook constitutive law is used for the metals. The model parameters follow the literature (Kittell et al. 2016; Frontán et al. 2012; Johnson and Cook 1983). The explosive, flyer plate, and base plate are discretized by 21,973, 67,529, and 75,573 RK nodes, respectively. For RK approximation, the normalized support sizes of 2.0 and 1.25 are respectively used for the explosive and metal plates. A node-based shock capturing scheme (Zhou 2016) with VC correction is employed to model shock wave propagation in the explosive and metals.

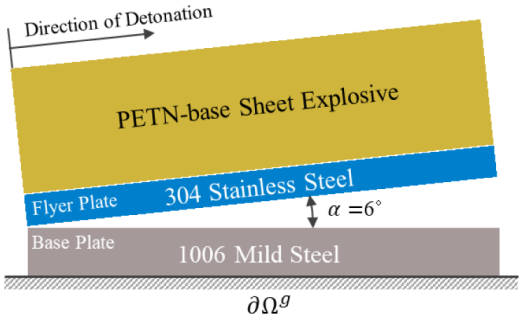

Figure 7. Model geometry of explosive welding (Baek et al. 2019).

As shown in Figure 8 (a), the explosion-induced shock propagation in the explosive and the flyer plate is well-captured by RKPM. The radial propagation of shock, which originates at the collision point of two metal pieces, indicates that the velocity of the moving collision point is slower than the sound speeds of two metals. The slower collision point velocity is a condition to produce metal jetting, which is considered necessary in explosive welding by sweeping out the impurities on the contact surfaces. The resulting metal jet is captured in the numerical result as shown in Figure 8 (d). The interfacial wave is gradually built up, as observed in an experiment (Bahrani et al. 1967) (see Figure 8 (d)), and enters a steady state where the length and height of waves match well with the experimental observation (Bahrani and Crossland 1964) (see Figure 8 (b) and (c)).

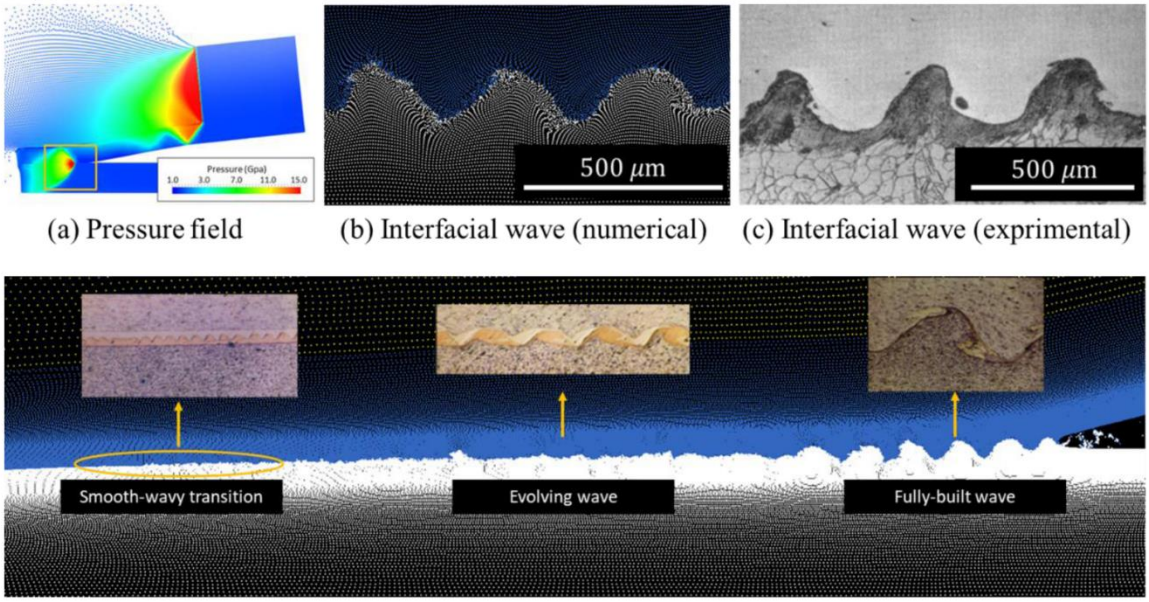

Figure 8. RKPM simulation (Baek et al. 2019) and experimental results (Bahrani and Crossland 1964) of explosive welding.

5. CONCLUSIONS

Extreme events often accompany severe material distortions, evolved from continuum deformation to discrete fragmentation, posing significant challenges to the continuum mesh-based finite element methods and the fully discrete-oriented discrete element method. RKPM, formulated using node-based RK discretization for controlling locality and continuity, if properly equipped with reliable (stable and convergent) nodal integration, offers a unique computational platform capable of modeling evolution of material deformation from continuum state to damaged and fragmented states under *one unified framework*. This paper introduced semi-Lagrangian RKPM with variationally consistent nodal integration VC-SNNI and NSNI stabilization for modeling problems with wide range of deformation and damage states. The simulation results have been validated and compared with experimentation observation, demonstrating the effectiveness and reliability of the proposed computational framework for modeling extreme events.

REFERENCES

Babuška, I., Banerjee, U., Osborn, J. E., & Li, Q. (2008). Quadrature for meshless methods. *International Journal for Numerical Methods in Engineering*, *76*(9), 1434-1470.

Baek J., Chen, J. S., Zhou, G., Arnett, K., Hillman, M., & Hegemier, G. (2019). "Modeling of Explosive Welding Using Semi-Lagrangian Reproducing Kernel Particle Method." Unpublished manuscript.

Bahrain, A. S., & Grassland, B. (1964). "Sixth Paper: Explosive Welding and Cladding: An Introductory Survey and Preliminary Results." *Proceedings of the Institution of Mechanical Engineers*, 179(1), 264-305.

Bahrani, A. S., Black, T. J., & Crossland, B. (1967). "The mechanics of wave formation in

explosive welding." *Proceedings of the Royal Society of London. Series A. Mathematical and Physical Sciences*, 296(1445), 123-136.

Beissel, S., & Belytschko, T. (1996). Nodal integration of the element-free Galerkin method. *Computer Methods in Applied Mechanics and Engineering*, *139*(1-4), 49-74.

Chen, J. S., Pan, C., Wu, C. T., & Liu, W. K. (1996). "Reproducing Kernel Particle Methods for Large Deformation Analysis of Nonlinear Structures." *Computer Methods in Applied Mechanics and Engineering*, 139, 195-227.

Chen, J. S., Wu, C. T., Yoon, S., & You, Y. (2001). A stabilized conforming nodal integration for Galerkin meshfree methods. *International Journal for Numerical Methods in Engineering*, 50(2), 435-466.

Chen, J. S., Zhang, X., & Belytschko, T. (2004). An implicit gradient model by a reproducing kernel strain regularization in strain localization problems. *Computer Methods in Applied Mechanics and Engineering*, *193*(27-29), 2827-2844.

Chen, J. S., & Wu, Y. (2007a). "Stability in Lagrangian and semi-Lagrangian reproducing kernel discretizations using nodal integration in nonlinear solid mechanics." *Advances in Meshfree Techniques*, 55-76.

Chen, J. S., Hu, W., Puso, M. A., Wu, Y., & Zhang, X. (2007b). Strain smoothing for stabilization and regularization of Galerkin meshfree methods. *Meshfree methods for partial differential equations III*, 57-75. Springer, Berlin, Heidelberg.

Chen, J. S., Chi, S. W., Lee, C. H., Lin, S. P., Marodon, C., Roth, M. J., & Slawson, T. R. (2011). "A Multiscale Meshfree approach for Modeling Fragment Penetration into Ultra-Strength Concrete." *Technical Report ERDC/GSL TR-11-35*. Vicksburg, MS: U.S. Army Engineer Research and Development Center.

Chen, J. S., Hillman, M., & Rüter, M. (2013). "An Arbitrary Order Variationally Consistent Integration Method for Galerkin Meshfree Methods." *International Journal for Numerical Methods in Engineering*, 95, 387-418.

Chen, J. S., Hillman, M., & Chi, S. W. (2017). "Meshfree Methods: Progress Made after 20 Years." *Journal of Engineering Mechanics*, 143(4), 04017001.

Chi, S. W., Chen, J. S., Hu, H. Y., & Yang, J. P. (2013). A gradient reproducing kernel collocation method for boundary value problems. *International Journal for Numerical Methods in Engineering*, *93*(13), 1381-1402.

Chi, S. W., Lee, C. H., Chen, J. S., & Guan, P. C. (2015). "A level set enhanced natural kernel contact algorithm for impact and penetration modeling." *International Journal for Numerical Methods in Engineering*, 102(3-4), 839-866.

Dolbow, J., & Belytschko, T. (1999). Numerical integration of the Galerkin weak form in meshfree methods. *Computational Mechanics*, *23*(3), 219-230.

Duan, Q., Li, X., Zhang, H., & Belytschko, T. (2012). "Second-order accurate derivatives and integration schemes for meshfree methods." *International Journal of Numerical Methods in Engineering*, 92(4), 399–424.

Frontán, J., Zhang, Y., Dao, M., Lu, J., Gálvez, F., & Jérusalem, A. (2012). "Ballistic performance of nanocrystalline and nanotwinned ultrafine crystal steel." *Acta Materialia*, 60(3), 1353-1367.

Guan, P. C., Chen, J. S., Wu, Y., Teng, H., Gaidos, J., Hofstetter, K., & Alsaleh, M. (2009). "Semi-Lagrangian reproducing kernel formulation and application to modeling earth moving operations." *Mechanics of Materials*, 41(6), 670-683.

Guan, P. C., Chi, S. W., Chen, J. S., Slawson, T. R., & Roth, M. J. (2011). "Semi-Lagrangian

reproducing kernel particle method for fragment-impact problems." *International Journal of Impact Engineering*, 38(12), 1033-1047.

Hegemier, G., Seible, F., Arnett, K., Rodriguez-Nikl, T., Oesterle, M., Wolfson, J., Gram. M., & Clark, A. (2006). "The UCSD blast simulator." *Proc., 77th shock and Vibration Symposium*, Arvonia, VA SAVIAC, 1-10.

Hillman, M., & Chen, J. S. (2016). "An accelerated, convergent, and stable nodal integration in Galerkin meshfree methods for linear and nonlinear mechanics." *International Journal for Numerical Methods in Engineering*, 107(7), 603-630.

Huang, T. H., Chen, J. S., Wei, H., Roth, M. J., Sherburn, J. A., Bishop, J. E., Tupec, M. R., & Fang, E. H. (2019a). "A MUSCL-SCNI approach for meshfree modeling of shock waves in fluids." *Computational Particle Mechanics*. https://doi.org/10.1007/s40571-019-00248-x.

Huang, T. H., Wei, H., Chen, J. S., & Hillman, M. C. (2019b). "RKPM2D: an open-source implementation of nodally integrated reproducing kernel particle method for solving partial differential equations." *Computational Particle Mechanics*, https://doi.org/10.1007/s40571-019-00272-x.

Johnson, G. R. (1983). "A constitutive model and data for materials subjected to large strains, high strain rates, and high temperatures." *Proc. 7th Inf. Sympo. Ballistics*, 541-547.

Kittell, D. E., Cummock, N. R., & Son, S. F. (2016). "Reactive flow modeling of small scale detonation failure experiments for a baseline non-ideal explosive." *Journal of Applied Physics*, 120(6), 064901.

Liu, G. R., Dai, K. Y., & Nguyen, T. T. (2007). "A smoothed finite element method for mechanics problems." *Computational Mechanics*, 39(6), 859–877.

Liu, W. K., Jun, S., & Zhang, Y. F. (1995). "Reproducing kernel particle methods." *International Journal for Numerical Methods in Fluids*, 20(8-9), 1081-1106.

Marsh, S. P. (1980). *LASL shock Hugoniot data (Vol. 5)*. University of California Press.

Puso, M. A., Chen, J. S., Zywicz, E., & Elmer, W. (2008). Meshfree and finite element nodal integration methods. *International Journal for Numerical Methods in Engineering*, *74*(3), 416-446.

Ren, X., Chen, J. S., Li, J., Slawson, T. R., & Roth, M. J. (2011). "Micro-cracks informed damage models for brittle solids." *International Journal of Solids and Structures*, 48(10), 1560-1571.

Roth, M. J., Chen, J. S., Danielson, K. T., & Slawson, T. R. (2016). "Hydrodynamic meshfree method for high-rate solid dynamics using a Rankine–Hugoniot enhancement in a Riemann-SCNI." framework. *International Journal for Numerical Methods in Engineering*, 108(12), 1525-1549.

Sherburn, J. A., Roth, M. J., Chen, J. S., & Hillman, M. (2015). "Meshfree modeling of concrete slab perforation using a reproducing kernel particle impact and penetration formulation." *International Journal of Impact Engineering*, 86, 96-110.

Taylor, G. I. (1948). "The use of flat-ended projectiles for determining dynamic yield stress I. Theoretical considerations." *Proceedings of the Royal Society of London. Series A. Mathematical and Physical Sciences*, 194(1038), 289-299.

von Neumann, J., & Richtmyer, R. D. (1950). "A method for the numerical calculation of hydrodynamic shocks." *Journal of Applied Physics*, 21(3), 232-237.

Wei, H, Chen, J. S., Beckwith, H., & Baek, J. (2019). "A Naturally Stabilized Semi-Lagrangian Meshfree Formulation for Multiphase Porous Media with Application to Landslide Modeling." *Journal of Engineering Mechanics*, 10.1061/(ASCE)EM.1943-7889.0001729.

Wilkins, M. L., & Guinan, M. W. (1973). "Impact of cylinders on a rigid boundary." *Journal of Applied Physics*, 44(3), 1200-1206.

Zhou, G. (2016). "A Reproducing Kernel Particle Method Framework for Modeling Failure of Structures Subjected to Blast Loadings." Doctoral Dissertation. UC San Diego.